Reduced finite element modelling and closed-loop control of pneumatic-driven soft continuum robots

Paul Chaillou[1*], Jialei Shi[2*], Alexandre Kruszewski[1], Isabelle Fournier[3], Helge A. Wurdemann[2], Christian Duriez[1]

***Abstract*— The introduction of soft robots has led to the development of inherently safe and flexible interventional tools for medical applications, when compared to their traditionally rigid counterparts. In particular, robot-assisted surgery is one of the medical applications that benefits from the inherent properties of soft instruments. However, robust control and reliable manipulation of soft tools remain challenging. In this paper, we present a new method based on reduced finite element method model and closed-loop inverse kinematics control for a fiber-reinforced soft robot. The highly flexible, pneumatically driven soft robot has three fully fiber-reinforced chamber pairs. The outer diameter is 11.5 mm. An inner working channel of 4.5 mm provides a free lumen for *in-vivo* cancer imaging tools during minimally invasive interventions. Here, the manipulator is designed in order to retrieve a tissue biopsy which can then be investigated for cancerous tissue. Simulation and experimental results are compared to validate the model and control methods, using one-module and two-module robots. The results show a real-time control is achievable using the reduced model. Combing the closed-loop control, the median position tracking errors are generally less than 2 mm.**

I. Introduction

For a long time, one way of ensuring positioning accuracy in robotics included the increase of stiffness in an articulated robot structure. But the metrics used, especially absolute positioning in space, were derived from use cases in industrial environments. In these settings, traditional robotic arms were made of rigid materials. For surgical robotics applications, the environment is fundamental different and the metrics have naturally evolved, giving a particularly interesting use case for soft robots. The need for performance, however, remains, which is sometimes challenging to obtain.

In this paper, we focus on a use case involving a soft robot for an automatic scanning tool during a laparoscopic procedure. To guarantee a precise scanning procedure, the robot requires a good *relative* positioning accuracy of its tip with respect to an organ surface. At the same time, this interventional application inside the human body demands an inherently safe robotic tool, which advocates for the usage of inherently soft materials. The challenge is to increase the *relative* positioning accuracy for a robotic manipulator made of soft material. Hence, the contribution of this paper lies in a new method based on reduced finite element method (FEM) model and its closed-loop inverse kinematics control, adapted for a fiber-reinforced soft robot for laparoscopy.

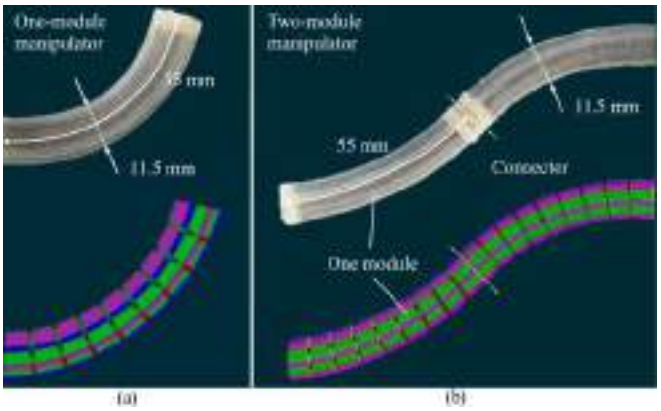

Fig. 1. The physical (top) and modelled (bottom) (a) one-module and (b) two-module soft manipulators in SOFA.

A. Background

Compared to rigid-link robots, soft continuum robots have a variety of design morphology and actuation principles [1]. The generalisation of a kinematic or dynamic modelling framework for soft robots is challenging [2]. One prominent modelling approach is the constant curvature (CC) model. The curvature along the back bone of a soft manipulator is assumed to be constant. Hence, the kinematic shape can be described by the curve length, curvature and out-of-plane angle [3]. The CC model can be extended to a piece-wise constant curvature (PCC) model, where a continuum robot is discretised into sections. Each section has a constant curvature [4]. In such way, a robot can have sections of different curvatures [5]. Based on the (P)CC assumptions, the dynamics model can be established, e.g., considering a robot is composed of virtual prismatic or revolute joints [6]. In addition, general variable curvature models have been explored, for instance, the Cosserat rod models [7], [8], the piecewise constant strain model [9], the beam mechanics [10] or FEM models [11]. As some approaches are computationally expensive, the shape interpolation [12] technique or reduced-order models have been explored [13] to improve efficiency.

Once the forward kinematics or dynamics models are

*Both authors contributed equally to this manuscript. This work is supported by the Engineering and Physical Sciences Research Council (grant numbers: EP/S014039/1, EP/V01062X/1), the UCL Dean's Prize, UCL Mechanical Engineering, and the China Scholarship Council.

[1]Paul Chaillou, Alexandre Kruszewski and Christian Duriez are with the University of Lille, Inria, CNRS, Centrale Lille, UMR 9189 CRIStAL, F-59000 Lille, France. e-mail: christian.duriez@inria.fr

[2]Jialei Shi and Helge A. Wurdemann are with the Department of Mechanical Engineering, University College London, UK. e-mail: h.wurdemann@ucl.ac.uk

[3]Isabelle Fournier is with the University of Lille, Inserm, CHU Lille, U1192-Protéomique Réponse Inflammatoire Spectrométrie de Masse-PRISM, Lille F-59000, France.

determined, the model-based inverse control can be implemented. Based on the (P)CC assumption, analytical inverse approaches can be calculated, for instance, via the closed form [14] or the differential Jacobian [15]. Della Santina *et. al* described dynamic impedance control when a soft robot is in physical interaction with the environment [16]. A real-time simulation and control method of soft robots with self-collisions is proposed in [17], based on a reduced-order FEM and implemented using SOFA [18]. Alternatively, the optimisation-based method can be used, e.g., constructing the initial conditions by including the actuation variables, the shooting method can solve the inverse control by minimising the errors of the boundary based on the Cosserat rod model [19]. Apart from model-based inverse control, learning approaches can be advantageous to deal with the un-modelled uncertainties and external disturbances [20]. Those modelling and control advances have facilitated the development of soft robots. In particular, the medical sector has emphasised increasing levels of autonomy to achieve safe and efficient robot-assisted surgeries [21]. In this case, robust and reliable control and manipulation of medical soft robots are of paramount importance.

B. Contribution and outline

In this paper, we first present the design of a highly flexible, pneumatically driven soft continuum robot, which is a miniaturised version of the STIFF-FLOP design [14]. The robot has three fully fiber-reinforced chamber pairs. Made of sewing thread, this fiber avoids the radial expansion. The outer diameter is 11.5 mm. An inner working channel of 4.5 mm provides a free lumen for *in-vivo* cancer imaging tools during minimally invasive interventions in cancer surgery. Here, a device is introduced through the inner free channel of the manipulator in order to retrieve a digital biopsy thanks to the molecular analysis of tumor and peri-tumoral tissues using a mass spectrometry based technology, the SpiderMass [22]. We then present the formulation of a reduced FEM model with the open-loop and closed-loop control, based on the hypothesis of the inextensibility of the fiber-reinforcement layer (see Fig. 1). The challenge is to use our new movement parameterization model to do real-time control. A comparison between the computational and experimental results validates our approach.

CROSS-SECTIONAL DIMENSION OF THE SOFT ROBOT

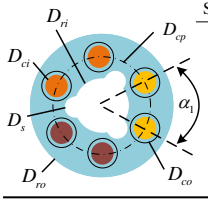

Symbol	Description	Value	Unit
D_{ro}	Diameter of the soft robot.	11.5	[mm]
D_{ri}	Diameter of the central lumen.	4.5	[mm]
D_{ci}	Inner diameter of the chambers.	1.5	[mm]
D_{cp}	Diameter of the chamber position.	8.0	[mm]
D_s	Diameter of the reserved slots.	1.5	[mm]
α_1	Angle between two adjacent chambers.	60.0	[deg]
D_{co}	Outer diameter of the chamber.	2.5	[mm]

Fig. 2. Overview of dimensions of the cross-sectional geometry. Two adjacent chambers are actuated as one pair, which have been marked in the same colour. One segment has an outer diameter of 11.5 mm, the actuation chambers have an inner diameter of 1.5mm. The free inner lumen has an inner diameter of 4.5 mm. The length of one module is 55 mm.

The remainder of the paper is organised as follows: Section II discusses the medical background for *in-vivo* cancer imaging and presents the design of the medical soft instruments. Section III then details the reduced FEM model with the open-loop and closed-loop inverse kinematics control. Section IV then reports the validation results from the simulation and experiments, using one-module and two-module robotic manipulators. Section V presents the discussions, and the conclusions are presented in Section VI.

II. REQUIREMENTS FOR IN-VIVO CANCER INTRAOPERATIVE IMAGING IN CANCER SURGERY USING SPIDERMASS TECHNOLOGY AND ROBOT DESIGN

A. Context : In-vivo cancer imaging

Surgery is essential and remains the first frontline treatment of solid cancers. In order to determine the exact extension of the cancer, to preserve non-cancerous tissue at most, robotic imaging may give useful informations the surgeon. Our envisioned technology is based on the mini-invasive real-time mass spectrometry (SpiderMass Technology) [23], within Minimally Invasive Surgery (MIS) context. Compared to traditional *in-vivo* imaging (CTscan, IRM) and margin verification systems (Histology and immunohistochemical analysis), which are time-consuming and limited, the SpiderMass Technology can analyse the cells in real-time and distinguish the different cell phenotypes therefore making possible to discriminate types, subtypes and grades of solid tumors [24]. It uses an optical fiber to bring the laser beam to the surface and a transfer line to bring the aerosol produced by the laser ablation up to the mass spectrometer for further analysis. Combining this real-time imaging technology with soft robots might result in a significant reduction in operation time and impact on the patient's health. Soft robots, due to their high dexterity and intrinsic safety, are very adapted to sensitive and narrow context, such as MIS. To product quick and accurate images, the point per point scanning have to be automatic, and soft properties may gives more security guarantee compared to rigid robot. This medical context leads to our design and to the constrains we want to satisfy. A hollow robot is also needed to be able to pass and protect the optic fiber and the suction tube of the SpiderMass system.

TABLE I

LIST OF MEDICAL TOOLS INSERTED THROUGH THE INNER WORKING CHANNEL OF THE SOFT ROBOT FOR *in-vivo* CANCER IMAGING.

Components	Diameter [mm]	Descriptions
Vacuum tube	1.5 mm	Retrieving the biopsy samples.
Actuation pipes*	1.0 mm	Three actuation pipes.
Depth sensor	1.0 mm	Checking the focal distance the laser ablation (three wires).
Optical fiber	0.7 mm	Ablating the organs.
Position sensor	1.0 mm	For the closed-loop control (one wire).

* The actuation pipes are passed through the preserved three slots parallel to the central working channel (see Fig. 2).

B. Design of one soft robotic module

Based on the introduced cancer imaging application, a pneumatically driven soft module is presented (see Fig. 1(a)), with an outer diameter of 11.5 mm (less than the diameter of the commercially available trocar port which has a diameter of 12 mm). An inner lumen of a 4.5 mm diameter is embedded. The length of one robot module is 55 mm. Connecting two robot modules in series results in a two-module robot which is highly flexible and dexterous (see Fig. 1(b)). The robot body is made of a low shore hardness silicone (Ecofex 00-50, SmoothOn). The robot has six fully fiber-reinforced chambers distributed evenly [25]. Two adjacent chambers are internally connected via a 1 mm silicone pipes and actuated as one pair. The robot fabrication can be referred to [14], [26]. To keep the inner lumen free for instrumental components (see Table. I), e.g., the optic fiber and sensor wires, three 1.5 mm diameter slots are preserved along the lumen to place the actuation pipes of a 1 mm diameter (see Fig. 2). For closed loop position control, the inner lumen offers sufficient space for an additional positioning sensor and depth sensor, so that the end effector is put at the focal distance of the surface to be analysed. Details of the cross-sectional geometries are shown in Fig. 2.

III. Modelling and Closed-Loop Control Method

The modelling and associated control methods require a trade-off between the accuracy and computational time. The quality of the control is impacted by the accuracy of the model, but in a feedback control scheme, the computation time is also of paramount importance. A high-frequency simulation will be beneficial for choosing control coefficients leading to a robust system, that is able to effectively resist perturbations and returns minimal modelling errors. In order to be able to compute real-time positioning, we derive a reduced FEM model to compute the elastic internal forces in a reduced *beam space*. In practice, we compute all internal forces and the impact of the actuation in the FEM space, but we solve the equilibrium of forces in this reduced space.

A. Modelling of the reduced model

1) Reduced beam kinematics: In beam theory, the motion of points follows certain assumptions. In particular, the cross-sections are assumed to be rigid, so the motion of any point in the beam can be parameterised by the central axis motions. This assumption of a rigid section is motivated by the use of fiber-reinforced chambers in the design. We use this beam kinematics to reduce the size of the motion coordinates of the model. To model forces on the soft robot module, we use a 3D FEM model, meshed with nodes. Then, the position of any nodes of the FEM can be deduced from the degrees of freedom (DOFs) of the beam. This yields in (1).

$$x = A(q) \tag{1}$$

where x denotes position of all nodes (denoted by p_n) of the FEM mesh, and q denotes position of the beam's DOFs (see Fig. 3). $A(q)$ creates a static link between the FEM nodes and beam, i.e., the position of the FEM points is static in the beam frame. For each point of the FEM, we associate a barycentric reference $R_{bary}(p_n, t)$ by interpolation

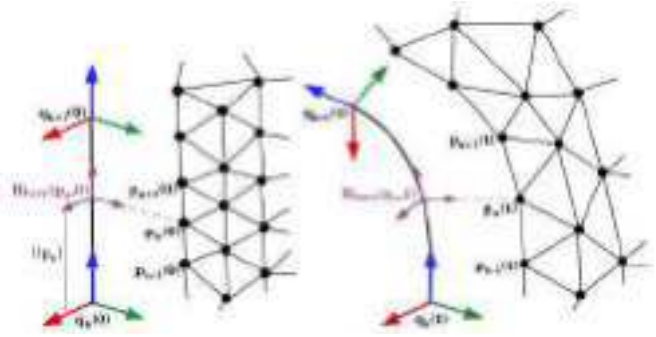

Fig. 3. Scheme of the link between the FEM nodes p_n and the beam DOF positions q_k.

$$R_{bary}(p_n, t) = slerp(q_k(t), q_{k+1}(t), l(p_n)) \tag{2}$$

where q_k is the position of the kth DOF of the beam, and $slerp()$ is the interpolation function for position and orientation between two nodes of the beam. Details on the interpolation method are described in [27]. $l(p_n)$ is the function that associates the p_n nodes to the position of the barycentric reference between two beam nodes. In the barycentric reference associated to each point, the position of the node p_n of the FEM mesh is static and described by

$$p_n(t)_{R_{bary}(p_n,t)} = p_n(0)_{R_{bary}(p_n,0)} \tag{3}$$

This models the fiber around the pneumatic cavities. As the distance between the FEM point and the beam node is fixed, the FEM mesh does not expand laterally due to fiber constraints. Expressing $p_n(t)$ in the global frame yields

$$R_{bary}(p_n, t)^{-1} p_n(t)_{Abs} = R_{bary}(p_n, 0)^{-1} p_n(0)_{Abs} \tag{4}$$

The subscript Abs refers to the absolute position in the global frame. As such,

$$p_n(t)_{Abs} = R_{bary}(p_n, t) R_{bary}(p_n, 0)^{-1} p_n(0)_{Abs} \tag{5}$$

In practice, this link is made in the SOFA framework using *BeamAdapter* Plugin [28]. For a small displacement or speed, the derivatives of node position x from (1) are described by

$$dx = \frac{\partial A}{\partial q} dq \quad \text{and} \quad \frac{dx}{dt} = \frac{\partial A}{\partial q} \frac{dq}{dt} \tag{6}$$

2) Forces projection : To model the structural non-linear elasticity and the pneumatic actuation, we compute the force balance on a volume 3D FEM model. To bring the non-linear forces $f(x)$ of the FEM mesh to the DOFs of the beam, we use the principle of virtual works which is independent from the references. The virtual displacement dq (or dx in the FEM space) makes the forces to work, this yields

$$dW = dx^T f(x) = dq^T \tau(q) \tag{7}$$

with $\tau(q)$ as the internal forces, expressed in this reduced space. The Jacobian matrix J of the function $A(q)$ is

introduced to achieve the coordinate transformation by

$$J = \frac{\partial A}{\partial q} \text{ so with (6), it is obtained : } \; dx = Jdq \quad (8)$$

By using the Jacobian matrix from (8), the forces in the FEM space expressed in the beam space are

$$J^T f(x) = \tau(q) \quad (9)$$

In practice, a linearisation is computed at each step to compute the equilibrium.

$$\begin{aligned} J^T f(x+dx) &\approx J^T (f(x) + \frac{\partial f}{\partial x} dx) \\ &\approx J^T f(A(q)) + J^T \mathrm{K} J dq \end{aligned} \quad (10)$$

$\mathrm{K} = \frac{\partial f}{\partial x}$ is the non-linear stiffness of the structure computed by FEM. This forces equilibrium is solved at each time step in the SOFA simulation. For the dynamics, we may calculate the same kind of projection. However, the implicit integration scheme is dampening the dynamics at this frame rate.

B. Comparison with the full FEM model

To validate and to measure the performance gain, the reduced model is compared with a classical FEM model without any beam motion reduction. In this simulation, we model the impact of the reinforcement fiber using stiff springs. These springs are placed around the cavity in the FEM, to reproduce the effect of real fibers constraining lateral deformation of the module (i.e., preventing ballooning).

1) Elastic parameters: As the impact of the reinforcement fiber is directly modelled in the classical FEM, the equivalent Young's modulus of Ecofex 00-50 is 100 kPa. For the reduced model, the force projection introduces artificial stiffness in the simulation. This artificial rigidity may be due to the beam assumption, i.e., the cross-section is rigid. So, the shrinking effect of the cross-section is constrained. Hence, the Young's modulus in the reduced model is 83 kPa, derived from the gradient descent optimisation.

2) Accuracy comparison: To investigate the accuracy between the two modelling techniques, three tests were conducted. 0 to 100 kPa were applied to one, two and three chamber. The positioning comparison results are displayed in Fig. 4. Globally, the positioning properties of the two models are very similar. We may see that for very large deformations, the reduced model looks to introduce artificial rigidity, that may be due to the static cross-section assumption of the robot in the reduced model.

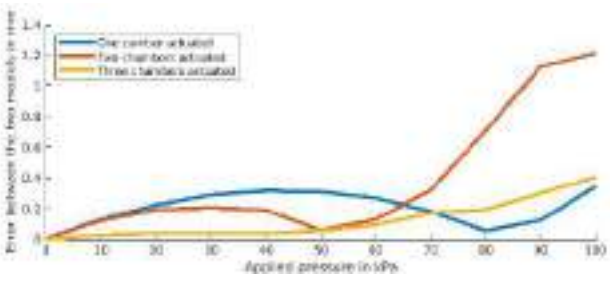

Fig. 4. Simulation comparisons between the classical and reduced FEM.

TABLE II

SUMMARY OF PERFORMANCE OF THE FULL & REDUCED FEM MODEL.

	1 module		2 modules	
	Time [s]	FPS*	Time [s]	FPS*
Full FEM	179.69 (0.83)	5.56 (0.02)	607.01 (0.90)	1.64 (0.01)
Reduced model	38.32 (2.28)	26.16 (1.48)	71.76 (0.71)	13.93 (0.14)

All the value are the mean value for 4 experiments, described with their standard deviation. (*FPS = Frame Per Second)

3) Computational performance comparison: To understand the computational expense, we run simulations in an open-loop control scenario, that drew a 40 mm diameter circle, as described in Experiment 2 (see Section IV-B). The simulations ran for 1000 iterations, each with a 0.1s time step. Each experiment ran 4 times. Table II summarises the mean time and FPS with the associated standard deviations. The computation of the reduced model is faster than the full FEM model. For the simulation of one module it is about 4 times faster. For the other simulations, it is about 8 times faster. Indeed, the complexity of the computation is different:

- for the full FEM model, most of the computation is dedicated to the factorization of the sparse FEM matrix system which has a theoretical complexity $\mathcal{O}(n^3)$.
- for the reduced model, most computational time is spent on the projection of matrix K in the reduced space ($J^T \mathrm{K} J$ shown in (10)) which has a linear complexity. The time to solve the equilibrium by factorization of the system is quick due to the fact that the size is small.

C. Inverse kinematics control

For the inverse kinematics control, we compute the inverse problem using an optimisation-based method [18], based on the reduced FEM model, using the available *SoftRobot.Inverse* Plugin in SOFA. In this way, the inverse control is open-loop because no feedback from the hardware (so $y_u = y_d$) is obtained. To accommodate un-modelled uncertainties, a closed-loop control is implemented using a proportional–integral (PI) controller. The desired position y_d is compensated by the current measured error y_e, so the

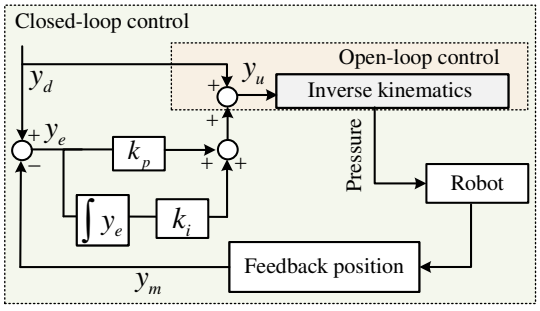

Fig. 5. The open-loop and closed-loop control scheme. y_d is the desired position, y_u is the input position to the inverse controller, and y_m is the measured position. For open-loop control, y_u equals y_d without feedback correction. While y_u is compensated by the feedback position using a PI controller in the closed-loop control.

demand y_u in the closed-loop control equals

$$y_u = y_d + k_p y_e + k_i \int_0^t y_e \mathrm{d}t \tag{11}$$

The open-loop and closed loop control schemes are summarised in Fig. 5. Please note that k_p and k_i are not scalars, instead, they have a diagonal form so the controller can use different gains to correct the position errors along three axes. In practice, the PI parameters are determined empirically.

IV. Computational Simulation and Experimental Validation Results

A. Experimental setup

The chamber pressure is regulated and monitored by proportional pressure regulators (Camozzi K8P). Pressurised air is supplied to the regulators by a compressor (HYUNDAI Model HY5508). The pressure regulators are controlled by an Arudino Due. The board sends PWMs ($0\sim 100\%$) which are proportionally converted to ($0\sim$ 10 V) analogue control voltages. An electromagnetic tracking system (NDI Aurora) monitors the tip (and the middle position) of the (two-module) robot using trackers. The positions are imported to SOFA as feedback information for closed-loop control. A PC runs SOFA including the simulation, inverse kinematics and closed-loop controller. SOFA sends out the real-time desired pressure to the Arduino Due board by serial communication.

B. Experimental protocols

Three sets of experiments were conducted to validate the reduced FEM model and the closed-loop and open-loop control methods. The desired position, measured position (from NDI trackers), simulated positions (from SOFA) and the chamber pressure were recorded. The fiber and vacuum pipes for Mass spectrometry were inserted to the central lumen during the experiments. The simulation steps in SOFA were set to 0.1 s.

Experiment 1 - Point-to-point control (one-module robot): A point table was implemented with desired points sent out one by one (see Fig. 6). The desired height is 55 mm and 60 mm on the right-hand and the left-hand x-y plane, respectively. To simulate a static condition, the desired positions were updated every 20 calculation steps. Both open-loop and closed-loop control were investigated. Each test repeated the point table 10 times.

Experiment 2 - Spatial trajectory tracking control (one-module robot): Four different trajectories were used to validate the open-loop and closed-loop control. Two circular trajectories with a diameter of 30 mm (C30) and 40 mm (C40), and two rectangular trajectories with a side length of 20 mm (R20) and 30 mm (R30), were chosen. The desired positions in the z-axis were kept as 55 mm. Each trajectory was repetitively tracked for 10 times.

Experiment 3 - Spatial trajectory tracking control (two-module robot): Two different trajectories were used to validate the modelling and control for a two-module robot. The trajectories included a circle shape with a diameter of 80 mm, and a rectangle shape with a side length of 60 mm. The desired positions in the z-axis were kept as 110 mm. Apart from the monitored tip position, an additional NDI tracker was embedded in the middle of the robot (see Fig. 9(a)). The robot's positions were tracked 10 times for each trajectory.

C. Simulation and experimental results

Results for Experiment 1: Fig. 6(a) visualises the results from the simulated positions (coloured in green), the desired positions (coloured in red), the measured positions from the open-loop control (coloured in magenta) and the measured positions from the closed-loop control (coloured in blue). From this figure, it can be seen that the errors from the open-loop controller become larger when heights of the desired points are 60 mm. Meanwhile, the green points show that the model can track the desired positions in the SOFA simulation environment. In general, the experimental results from the closed-loop control have the smallest errors.

The open-loop and closed-loop control are summarised in Fig. 6(b) and Fig. 6(c), respectively. The overall mean errors are 0.9 mm and 3.4 mm for the open-loop and closed-loop control. Fig. 6(b) shows that the maximum error of the open-loop control is 10.2 mm, which occurs when the robot approaches the furthest points, i.e., $[-10, 10, 60]$ mm. Compared to the results from the left-hand x-y plane ($x \leq$ 0 mm, $z = 60$ mm), the results from the right-hand x-y plane ($x \geq 0$ mm, $z = 55$ mm) have overall smaller errors, with the maximum mean error of 2.9 mm at $[10, 10, 55]$ mm. Fig. 6(c) reports the error details of the closed-loop control. By contrast, the errors are more consistent at different points, with an overall maximum error of 1.4 mm.

Results for Experiment 2: Fig. 7 reports and compares the recorded trajectory when the robot finished the first-time tracking. In general, compared to Figs. 7(b) and 7(c),

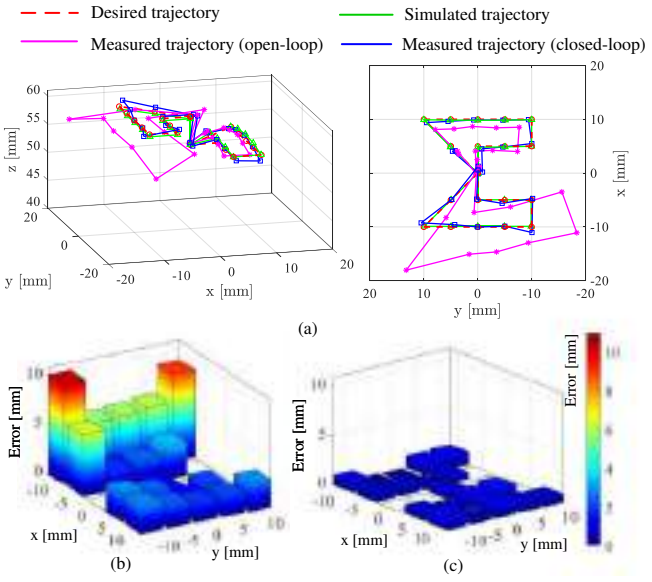

Fig. 6. Results for Experiment 1: (a) Comparison between the measured tip position, the simulated position and the desired position for the open-loop and closed-loop controller. The summarised mean absolute tip errors with respect to different desired points are shown in (b) and (c).

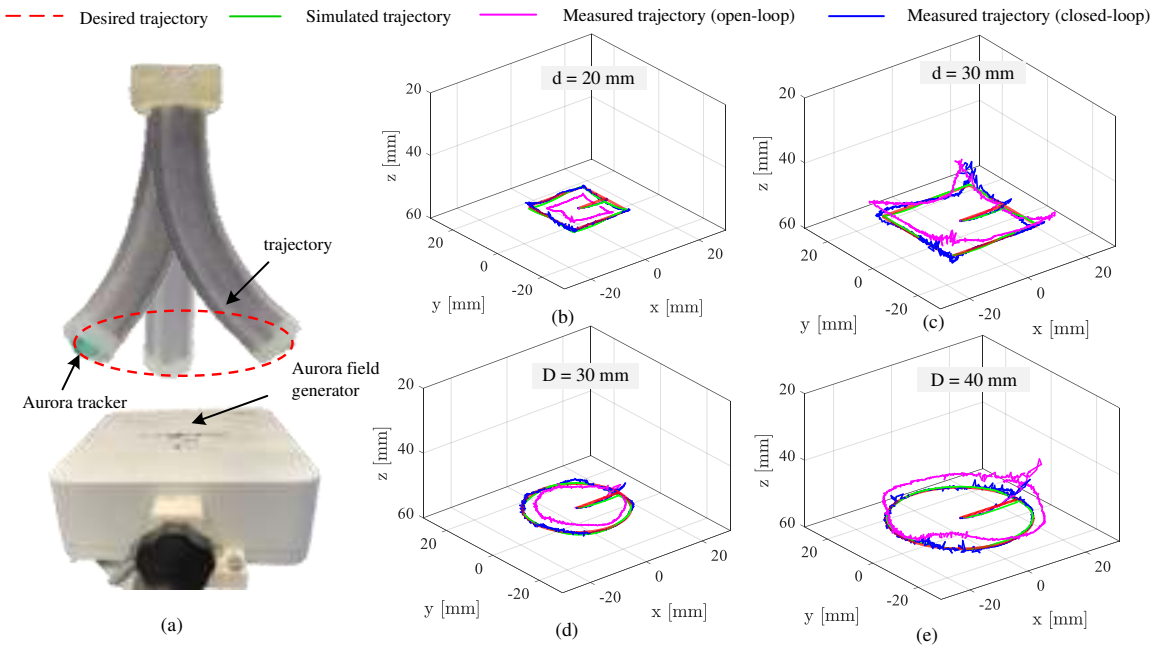

Fig. 7. Results for Experiment 2: Trajectory tracking performance of open-loop and the closed-loop control. (a) Measurement of the robot's trajectory. Results for (b) tracking a rectangle, with a side length of 20 mm, (c) tracking a rectangle, with a side length of 30 mm, (d) tracking a circle, with a diameter of 30 mm, and (e) tracking a circle, with a diameter of 40 mm.

Figs. 7(d) and 7(e) show the errors from the open-loop control become larger when tracking larger trajectories. Conversely, the closed-loop controller results in the robot consistently and stably following the desired trajectories. Furthermore, the summarised errors from the open-loop and closed-loop control are reported in Fig. 8 using box plots. In particular, the median errors from the closed-loop control are 0.8 mm, 1.2 mm, 0.7 mm, and 0.8 mm for R20, R30, C30 and C40, respectively. By contrast, the median errors from the open-loop control are 4.5 mm, 2.4 mm, 3.0 mm, and 4.8 mm for R20, R30, C30 and C40, respectively. Moreover, the open-loop control has smaller errors when the tracking shapes have smaller dimensions, e.g., shown in Figs. 8(a) and (c). The maximum errors increase when the trajectories become larger (see Figs. 8(b) and (d)).

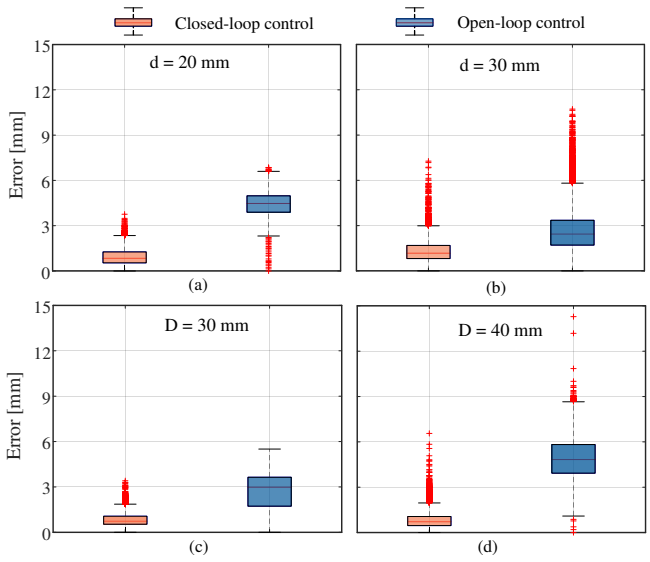

Fig. 8. Results for Experiment 2: Summarised tracking errors using box plots. Results for rectangles are shown in (a) and (b), with a width of 30mm and 40mm. The results for circles are shown in (c) and (d), with a radius of 15mm and 20mm. The central red marks, the bottom and top edges of the box indicate the median, the 25th and 75th percentiles, respectively. The outliers are plotted using the '+' symbol.

Results for Experiment 3: Fig. 9 reports trajectory tracking results for a two-module robot. The inverse kinematics controller shows effective and reliable performance as the circle and rectangle shapes can be tracked (see Figs. 9(b) and (c)), while the open-loop and closed-loop results have different accuracies. Similar to Fig. 7(c), Fig. 9(c) also shows that the error of the open-loop control becomes larger when the robot approaches any of the four corners of the rectangle. Furthermore, as shown in Fig. 10, the median closed-loop tip errors are 1.6 mm and 1.9 mm for the circular and rectangular shapes, respectively. By comparison, the median tip errors using the open-loop control are 6.9 mm and 7.9 mm for the circular and rectangular shapes, respectively.

V. Discussions

A. Discussions of the model and open-loop control

In Experiment 1, the results show that the robot can successfully follow the point-to-point command for both open-loop and closed-loop control. The accuracy of the open-loop control decreases when the robot travels further distances. Similar results are observed in Experiments 2 and 3, the open-loop control accuracy deteriorates under

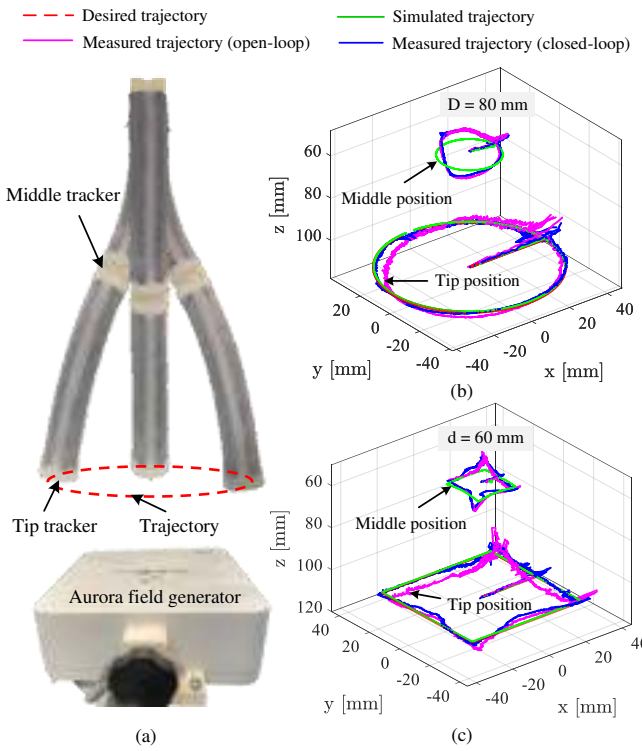

Fig. 9. Results for Experiment 3: Trajectory tracking of the open-loop and closed-loop control for a two-module robot. (a) Measurement of the trajectory. Tracking results for (b) a rectangular shape, with a side length of 60 mm, and (c) a circular shape, with a diameter of 80 mm.

larger desired trajectories, e.g., the non-outlier maximum errors increase from 5.5 mm (for C30) to 8.7 mm (for C40) for the one-module robot. This difference might result from the modelling accuracy as the open-loop control directly solves the inverse kinematics based on the established model. In this work, we assumed a linear material model with a constant Young's Modulus. This assumption becomes less effective when the robot undergoes larger deformation, as the silicone material shows a nonlinear strain-stress relationship [29]. As such, exploring nonlinear hyper-elastic models might improve the modelling accuracy and further mitigate the errors from the open-loop control. For instance, it was reported that the Neo-Hookean model could be used to model the fiber-reinforced bending actuator when the elongation is less than 50% [30]. Furthermore, the cross-sectional area will shrink when the robot elongates, in particular, when the material is incompressible, as reported in [31]. Considering this cross-sectional deformation in the reduced model could also improve the modelling accuracy.

B. Discussions of the closed-loop control

Experiments 1-3 show that the closed-loop control can reliably improve accuracy of the point-to-point and trajectory tracking performance. By introducing position feedback, the closed-loop control first can mitigate the inaccuracy of the material model discussed in Section V-A. It can then alleviate the un-modelled uncertainties, e.g., the potential

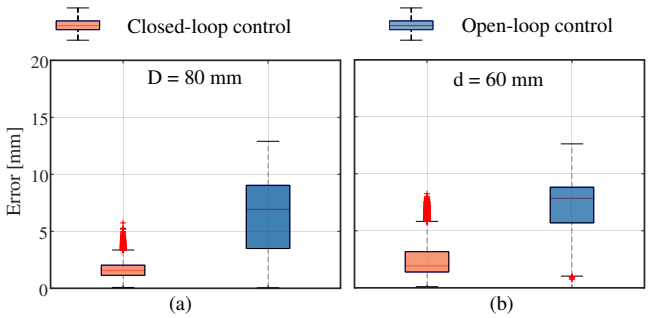

Fig. 10. Results for Experiment 3: Summarised tracking errors for (a) a circle with a diameter of 80 mm, (b) rectangle with a side length of 60 mm.

inconsistencies of the robot fabrication or errors for the pressure control. As shown in Fig. 11, the comparison of the actuation pressure for the open-loop and closed-loop control of the one-module robot for C40 circle tracking are reported. The dotted pressure curves are derived based on the model-based inverse kinematics, and the solid curves are the pressure values from the closed-loop control. The differences between two curves are the efforts that the closed-loop controller takes to correct the uncertainties. Although the closed-loop control can improve the control accuracy, it is worth mentioning that the position sensing needs additional sensors. Adding position sensors might be challenging for the targeted medical application. Improving the modelling accuracy can be helpful. In addition, exploring proprioceptive sensing is meaningful [32] for achieving a self-contained closed-loop control. Moreover, we focused on the quasi-static scenario in this work. However, dynamic behaviours were also observed during the point-to-point tests, indicating the consideration of a dynamic model that might improve the controlled manoeuvrability of the robot.

VI. Conclusions

Aiming at applying soft robots for cancer imaging in minimally invasive interventions, we first designed a flexible modular soft instrument prototype, with an outer diameter of

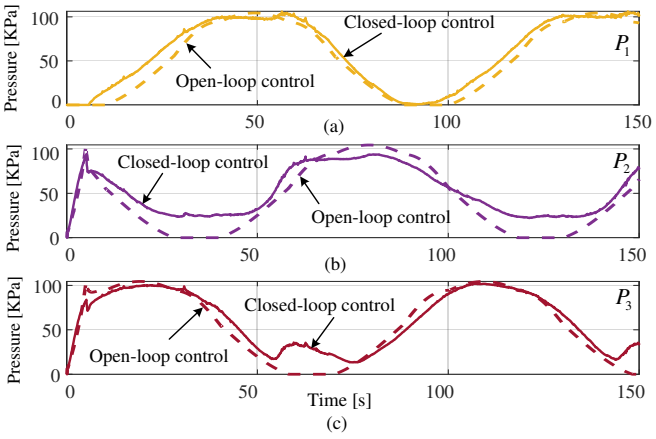

Fig. 11. Comparison of pressure values for open- and closed-loop control for the one-module robot following a 40 mm-diameter circular trajectory.

11.5 mm. The robot can be inserted through a commercially available 12 mm trocar port. The robot is equipped with an inner free lumen of a 4.5 mm diameter, which can accommodate the optic fiber and vacuum pipes for retrieving biopsies. In addition, two modules have been connected to achieve higher flexibility (see Fig. 1). We applied the reduced FEM technique to model and control both the one-module and two-module soft robots using SOFA. The simulation demonstrates performances of the reduced FEM is at least 4 times faster than a classical FEM model. The simulation and experiments were both conducted to further validate the reduced FEM model and inverse control. To compensate unmodelled uncertainties in the open-loop control and improve the control accuracy, we introduced the closed-loop control using position feedback.

In future work, we will first aim to improve the model accuracy which can further produce better open-loop control results, e.g., by introducing nonlinear hyper-elastic material models and considering the dynamics behaviour. In addition, we will integrate the soft instrument prototypes to the phantom and the SpiderMass device to develop and validate the proposed medical application.

REFERENCES

[1] D. Rus and M. T. Tolley, "Design, fabrication and control of soft robots," *Nature*, vol. 521, no. 7553, pp. 467–475, 2015.

[2] C. Armanini, C. Messer, A. T. Mathew, F. Boyer, C. Duriez, and F. Renda, "Soft robots modeling: a literature unwinding," *arXiv preprint arXiv:2112.03645*, 2021.

[3] R. J. Webster III and B. A. Jones, "Design and kinematic modeling of constant curvature continuum robots: A review," *The International Journal of Robotics Research*, vol. 29, no. 13, pp. 1661–1683, 2010.

[4] M. W. Hannan and I. D. Walker, "Kinematics and the implementation of an elephant's trunk manipulator and other continuum style robots," *Journal of Robotic Systems*, vol. 20, no. 2, pp. 45–63, 2003.

[5] T. Mahl, A. Hildebrandt, and O. Sawodny, "A variable curvature continuum kinematics for kinematic control of the bionic handling assistant," *IEEE Transactions on Robotics*, vol. 30, no. 4, pp. 935–949, 2014.

[6] R. K. Katzschmann, C. D. Santina, Y. Toshimitsu, A. Bicchi, and D. Rus, "Dynamic motion control of multi-segment soft robots using piecewise constant curvature matched with an augmented rigid body model," in *2019 2nd IEEE International Conference on Soft Robotics (RoboSoft)*, 2019, pp. 454–461.

[7] D. C. Rucker, B. A. Jones, and R. J. Webster III, "A geometrically exact model for externally loaded concentric-tube continuum robots," *IEEE Transactions on Robotics*, vol. 26, no. 5, pp. 769–780, 2010.

[8] J. Till, V. Aloi, and C. Rucker, "Real-time dynamics of soft and continuum robots based on Cosserat rod models," *The International Journal of Robotics Research*, vol. 38, no. 6, pp. 723–746, 2019.

[9] F. Renda, F. Boyer, J. Dias, and L. Seneviratne, "Discrete cosserat approach for multisection soft manipulator dynamics," *IEEE Transactions on Robotics*, vol. 34, no. 6, pp. 1518–1533, 2018.

[10] M. T. Chikhaoui, S. Lilge, S. Kleinschmidt, and J. Burgner-Kahrs, "Comparison of modeling approaches for a tendon actuated continuum robot with three extensible segments," *IEEE Robotics and Automation Letters*, vol. 4, no. 2, pp. 989–996, 2019.

[11] C. Duriez, "Control of elastic soft robots based on real-time finite element method," in *2013 IEEE International Conference on Robotics and Automation (ICRA)*, May 2013, pp. 3982–3987, iSSN: 1050-4729.

[12] S. M. H. Sadati, Z. Mitros, R. Henry, L. Zeng, L. d. Cruz, and C. Bergeles, "Real-time dynamics of concentric tube robots with reduced-order kinematics based on shape interpolation," *IEEE Robotics and Automation Letters*, vol. 7, no. 2, pp. 5671–5678, 2022.

[13] J. M. Gandarias, Y. Wang, A. Stilli, A. J. García-Cerezo, J. M. Gómez-de Gabriel, and H. A. Wurdemann, "Open-loop position control in collaborative, modular variable-stiffness-link (VSL) robots," *IEEE Robotics and Automation Letters*, vol. 5, no. 2, pp. 1772–1779, 2020.

[14] H. Abidi, G. Gerboni, M. Brancadoro, J. Fras, and et al., "Highly dexterous 2-module soft robot for intra-organ navigation in minimally invasive surgery," *The International Journal of Medical Robotics and Computer Assisted Surgery*, vol. 14, no. 1, p. e1875, 2018.

[15] B. Jones and I. Walker, "Kinematics for multisection continuum robots," *IEEE Transactions on Robotics*, vol. 22, no. 1, pp. 43–55, 2006.

[16] C. Della Santina, R. K. Katzschmann, A. Bicchi, and D. Rus, "Model-based dynamic feedback control of a planar soft robot: trajectory tracking and interaction with the environment," *The International Journal of Robotics Research*, vol. 39, no. 4, pp. 490–513, 2020.

[17] O. Goury, B. Carrez, and C. Duriez, "Real-time simulation for control of soft robots with self-collisions using model order reduction for contact forces," *IEEE Robotics and Automation Letters*, vol. 6, no. 2, pp. 3752–3759, 2021.

[18] C. Duriez, E. Coevoet, F. Largilliere, T. Morales-Bieze, and et al., "Framework for online simulation of soft robots with optimization-based inverse model," in *2016 IEEE International Conference on Simulation, Modeling, and Programming for Autonomous Robots (SIMPAR)*. IEEE, 2016, pp. 111–118.

[19] J. Till, C. E. Bryson, S. Chung, A. Orekhov, and D. C. Rucker, "Efficient computation of multiple coupled cosserat rod models for real-time simulation and control of parallel continuum manipulators," in *2015 IEEE international conference on robotics and automation (ICRA)*. IEEE, 2015, pp. 5067–5074.

[20] T. George Thuruthel, E. Falotico, M. Manti, A. Pratesi, M. Cianchetti, and C. Laschi, "Learning closed loop kinematic controllers for continuum manipulators in unstructured environments," *Soft Robotics*, vol. 4, no. 3, pp. 285–296, 2017.

[21] G.-Z. Yang, J. Cambias, K. Cleary, E. Daimler, and et al., "Medical robotics—regulatory, ethical, and legal considerations for increasing levels of autonomy," p. eaam8638, 2017.

[22] B. Fatou, M. Wisztorski, C. Focsa, M. Salzet, M. Ziskind, and I. Fournier, "Substrate-mediated laser ablation under ambient conditions for spatially-resolved tissue proteomics," *Scientific reports*, vol. 5, no. 1, pp. 1–14, 2015.

[23] N. Ogrinc, A. Kruszewski, P. Chaillou, S. Philippe, C. Lagadec, M. Salzet, C. Duriez, and I. Fournier, "Robot-Assisted SpiderMass for in vivo real-time topography mass spectrometry imaging," *Analytical Chemistry*, vol. 93, Oct. 2021.

[24] P. Saudemont, J. Quanico, Y.-M. Robin, A. Baud, and et al., "Real-Time molecular diagnosis of tumors using water-assisted laser desorption/ionization mass spectrometry technology," *Cancer Cell*, vol. 34, no. 5, pp. 840–851.e4, Nov. 2018.

[25] J. Fraś, J. Czarnowski, M. Maciaś, J. Główka, M. Cianchetti, and A. Menciassi, "New STIFF-FLOP module construction idea for improved actuation and sensing," in *2015 IEEE International Conference on Robotics and Automation (ICRA)*, 2015, pp. 2901–2906.

[26] J. Shi, W. Gaozhang, and H. A. Wurdemann, "Design and characterisation of cross-sectional geometries for soft robotic manipulators with fibre-reinforced chambers," in *2022 IEEE 5th International Conference on Soft Robotics (RoboSoft)*, 2022, pp. 125–131.

[27] J.-s. Ahn, W.-j. Chung, and C.-d. Jung, "Realization of orientation interpolation of 6-axis articulated robot using quaternion," *Journal of Central South University*, vol. 19, no. 12, pp. 3407–3414, 2012.

[28] F. Jourdes, B. Valentin, J. Allard, C. Duriez, and B. Seeliger, "Visual haptic feedback for training of robotic suturing," *Frontiers in Robotics and AI*, vol. 9, p. 800232, Feb. 2022.

[29] L. Marechal, P. Balland, L. Lindenroth, F. Petrou, C. Kontovounisios, and F. Bello, "Toward a common framework and database of materials for soft robotics," *Soft Robotics*, vol. 8, no. 3, pp. 284–297, 2021.

[30] P. Polygerinos, Z. Wang, J. T. Overvelde, K. C. Galloway, and et al., "Modeling of soft fiber-reinforced bending actuators," *IEEE Transactions on Robotics*, vol. 31, no. 3, pp. 778–789, 2015.

[31] M. Gazzola, L. Dudte, A. McCormick, and L. Mahadevan, "Forward and inverse problems in the mechanics of soft filaments," *Royal Society Open Science*, vol. 5, no. 6, p. 171628, 2018.

[32] Y. Toshimitsu, K. W. Wong, T. Buchner, and R. Katzschmann, "SoPrA: Fabrication dynamical modeling of a scalable soft continuum robotic arm with integrated proprioceptive sensing," in *2021 IEEE/RSJ International Conference on Intelligent Robots and Systems (IROS)*, 2021, pp. 653–660.